

AS03 Investigating the Merger-Free Co-Evolution of Black Holes

Abstract

It is becoming increasingly clear that significant growth of supermassive black holes (SMBHs) is possible in the absence of galaxy mergers. However, the effects of this merger-free black hole growth on galaxy-black hole co-evolution are as yet unknown. To this end, I study a candidate sample of 26 visually selected bulgeless SMBH host galaxies, since a merger-free history manifests itself in a bulgeless morphology. Of this sample, parametric morphological fitting confirms that 24 of these galaxies show no sign of mergers, with 13 containing a non-merger driven pseudo-bulge contribution of $> 15\%$, and 11 bulge contributions of $< 15\%$. Out of these 24, X-ray data indicate that 15 objects host confirmed SMBHs, the other 8 are potentially star formation galaxies. The existence of at least 15 (and possibly 24) mergerless SMBH hosts results supports earlier findings that significant BH growth is compatible with mergerless evolution and confirms this result to higher redshifts (up to $z \sim 1$). Furthermore, mass relations between M_{BH} and M_{host} , and M_{BH} and pseudo-bulge M_{bulge} , are consistent with established relations for merger-dominated classical bulges and elliptical galaxies, suggesting that mergers need not be fundamental to galaxy black-hole coevolution. Additionally, I observe a tentative increase of M_{BH}/M_{bulge} with decreasing redshift, which agrees with earlier results for $z \sim 0$.

1 INTRODUCTION

One of the central topics in modern galaxy evolution theory concerns the influence of mergers on the evolution of galaxies, and the role of supermassive black holes in this process. According to the predominant paradigm, mergers are believed to form galaxies hierarchically, driving the growth of SMBHs in this process [1] [2] [3]. However, an increasing body of evidence suggests that mergers are not required to grow a central black hole at any $z < 3$ [4] [5] [6] [7]. In order to quantify the effect of such merger-free processes on black hole growth, a sample of SMBHs in galaxies with no history of mergers will be required.

This evolutionary history can partially be traced through a galaxy's morphology [8]. For instance, spiral galaxies are dynamically cold systems, consisting of a disk of stars and interstellar medium, rotating fairly uniformly around the galactic centre. Elliptical galaxies on the other hand, are dynamically hot with stellar motions unordered, and have a steeper density profile than disks. Major mergers between spiral galaxies are known to result in el-

lipticals. Physically, when two rotating disks approach each other at an angle, gravitational interactions will violently mix up the stars and destroy the uniform disk motions, resulting in an elliptically shaped galaxy with randomly distributed stellar motions. Similarly, minor mergers of a larger disk galaxy with a smaller companion invariably produce a central elliptical component called a bulge. Thus, as a bulgeless morphology implies an evolutionary history free of mergers and other violent processes.

Most (if not all) galaxies host a central supermassive black hole (SMBH, $m_{BH} \gtrsim 10^6 M_\odot$) [9] [10]. Active galactic nuclei (AGN) are unusually bright regions in the centres of galaxies, believed to consist of radiation emitted by such an accreting SMBH [11][12]. Their exceptional brightness allows them to be clearly visible even in bright galactic centres, providing a means of SMBH detection as well as a handle on properties such as BH mass. It is often claimed that central SMBHs have accumulated their sizeable masses from galaxy mergers, either through merging with other galaxies' SMBHs, or through additional accre-

tion fueled by violent disruption of galactic matter in the merger process. In support of this hypothesis, strong correlations exist between black hole mass and bulge properties [13][9][14][15], suggesting close co-evolution in the case of these merger-dominated objects.

However, in light of the aforementioned recent suggestions of merger-free black hole growth, I aim to investigate whether similar galaxy-black hole relations exist in a sample of mergerless galaxies. A sample of such bulgeless merger-free AGN hosts has previously been identified by Simmons et al. 2013 [7] for $z \sim 0$. In this project I expand on this sample, presenting 26 bulgeless AGN host candidates, and extend the depth up to higher redshifts of $z \sim 1$. This corresponds to a time when the universe was around 6 Gyr old, allowing for the study of merger-free black hole growth over a longer period of cosmic time.

Section 2 describes the imaging and selection of the candidate sample and data, as well as X-ray AGN selection. Section 3 describes methods used in this project, and in particular the process of parametric morphological fitting. In Section 4 I present the results of this process, and in Section ??, I explain how I obtained galaxy and black hole masses. Section 5 explores the implications of the results of this project for galaxy black hole co-evolution. Throughout this project, I have assumed $H_0 = 71 \text{ km s}^{-1} \text{ Mpc}^{-1}$, $\Omega_M = 0.27$ and $\Omega_\Lambda = 0.73$, to retain consistency with earlier data used in this project.

2 IMAGE AND DATA SELECTION

2.1 Data

2.1.1 Optical AGN and Host Galaxy Imaging

Reliable bulge-disk and point-source decomposition of AGN host galaxies at redshifts $z \gtrsim 0.1$ requires deep space-based observations in a field with excellent multi-wavelength data for selection of AGN. This project thus uses images taken from the Great Observatories Origins Deep Survey (GOODS) [16] with the Advanced Camera for Surveys (ACS) on the *Hubble Space Telescope* (HST). The survey covered roughly 320 square arcminutes in

two fields, centered on the *Hubble* Deep Field North (HDF-N) and the *Chandra* Deep Field South (CDF-S) [17]. Observations encompass optical and near-infrared imaging in the F435W, F606W, F775W, and F850LP passbands, also referred to as B , V , I , and z' .

In order to maximise any possible bulge flux, it is generally preferable to use the reddest available imaging, as classical bulges are no longer forming stars and thus contain redder stellar populations [18]. However, because the reddest ACS z' -band has higher background noise and a noisier PSF (for PSF see Section 3.3.2), this project focuses on the next reddest, i.e. I -band imaging.

2.1.2 X-ray data

X-ray data in the soft (0.5 - 2 keV) and hard (2 - 8 keV) bands were taken from the *Chandra* point-source catalogs of Alexander et al. [19] and Xue et al. [20] for the HDF-N and CDF-S, respectively. These fields contain some of the deepest X-ray observations, at 2 Ms and 4 Ms respectively, providing more than adequate depth to detect AGN emission at all redshifts considered in this project.

The X-ray point sources were matched to optical sources by Cardamone et al. 2008 [21] and Bauer et al. 2002 [22], 2004 [23] using a maximum likelihood algorithm.

2.1.3 Redshifts

The analyses in this project require reliable distance measurements in the form of spectroscopic redshifts. Redshifts used in this project were obtained from Wirth et al. 2004 [24], Cowie et al. 2004 [25] and Barger et al [26].

2.2 Sample selection

2.2.1 Visual inspection

The sample of candidate bulgeless consists of 26 AGN host galaxies, and was selected by B. Simmons after visual inspection of 288 optical matches to X-ray point sources. The 26 candidate colour images are displayed in Figure 1. As explained in Section 4, objects 50006849 and 90044623 were rejected from the sample. From visual inspection it is evident that galaxy orientations vary from face-on to nearly edge-on, and span a range of colours. Addition-

ally, the sample contains both barred and unbarred disks and a variation in tightness of spiral windings. Thus, the analysis presented in this project should contain no significant bias towards a particular type of disk morphology.

2.3 AGN selection

In addition to AGN activity, star formation and X-ray binaries can also contribute to X-ray flux. In order to reject galaxies where these processes dominate X-ray emission, I classified objects according to their hard band X-ray luminosity and hardness ratios ($HR = \frac{H-S}{H+S}$, where H and S are the net count rates in the hard and soft band). Throughout the project I employed the following selection criteria, based on criteria in Szokoly et al 2004 [28]:

- **Unobscured AGN:** hard X-ray luminosity $L_x > 10^{42}$ erg/s and $HR \leq -0.2$
- **Obscured AGN:** hard X-ray luminosity $L_x > 10^{41}$ erg/s and $HR > -0.2$

Object 50002399 contains an unobscured AGN, and 14 others contain obscured AGN. The other 9 fall outside these categories. However, the faint flux limit of the deep X-ray images means that not all galaxies are expected to show clear indications of AGN activity from the X-ray emission alone. Parametric morphological fitting detects significant point sources for all 9 objects that fall outside the above selection criteria (see Table 2). As spurious point source detection in parametric fitting is fairly uncommon (e.g. Simmons & Urry 2008 [29] finds a maximum rate of 25 % in bulge-dominated sources), these 9 galaxies are retained in the sample of bulgeless AGN hosts, and shall be classified as “uncertain AGN”. All classifications are displayed in Figure 1.

3 METHODS AND FITTING

3.1 Methods

A considerable part of this project involved parametric morphological fitting with **GALFIT**. I wrote scripts in bash in order to automate parts of this process, such as running **GALFIT** automatically, and generating input files and catalogs. Some tasks regarding images, such

as creating bad pixel masks, and image scaling, required use of **IRAF** [30]. Throughout this project, I used **TOPCAT** [31] for handling datasets, as well as for computing and converting between astrophysical quantities. For the F-test described in AppendixB, I created scripts in the R programming language [32]. The remainder of this Section presents the details of parametric morphological fitting.

3.2 Motivation for parametric fitting

3.2.1 AGN can visually mimic bulges

As both AGN and bulges resemble an extended bright central region on the images, visual inspection may lead to an incorrect classification. Thus, in order to obtain a more certain measure of the presence of bulges or AGN, it is necessary to follow up this visual classification with a more secure way to separate AGN, disk and bulge. Additionally, a quantitative analysis will require measurements of bulge-to-total ratios. To this end, this project employs parametric morphological fitting of the candidate sample, to separate the AGN point source contribution from disks and spatially extended central bulges.

3.2.2 Distinguishing between classical bulges and pseudo-bulges

An important issue in the morphological classification of bulges concerns the distinction between bulges and pseudo-bulges. Classical bulges (sometimes simply called ‘bulges’) have a similar light distribution profile and obey similar parameter correlations to elliptical galaxies. As mentioned in Section 1, they are equally believed to result from minor mergers. Pseudo-bulges, on the other hand, have properties more akin to disks, including shallower light profiles than classical bulges (though often slightly steeper than disks, with typically $n \lesssim 2$). They are believed to be formed in internal processes such as relatively fast (but still cold) gas accretion, and from various strong disk instabilities such as bars and large-scale clumps. They are thus consistent with a merger-free history [33] [18]. As such, pseudo-bulges are admissible in our mergerless sample, and the term ‘bulgeless’ shall henceforth refer to galaxies lacking a classical bulge,

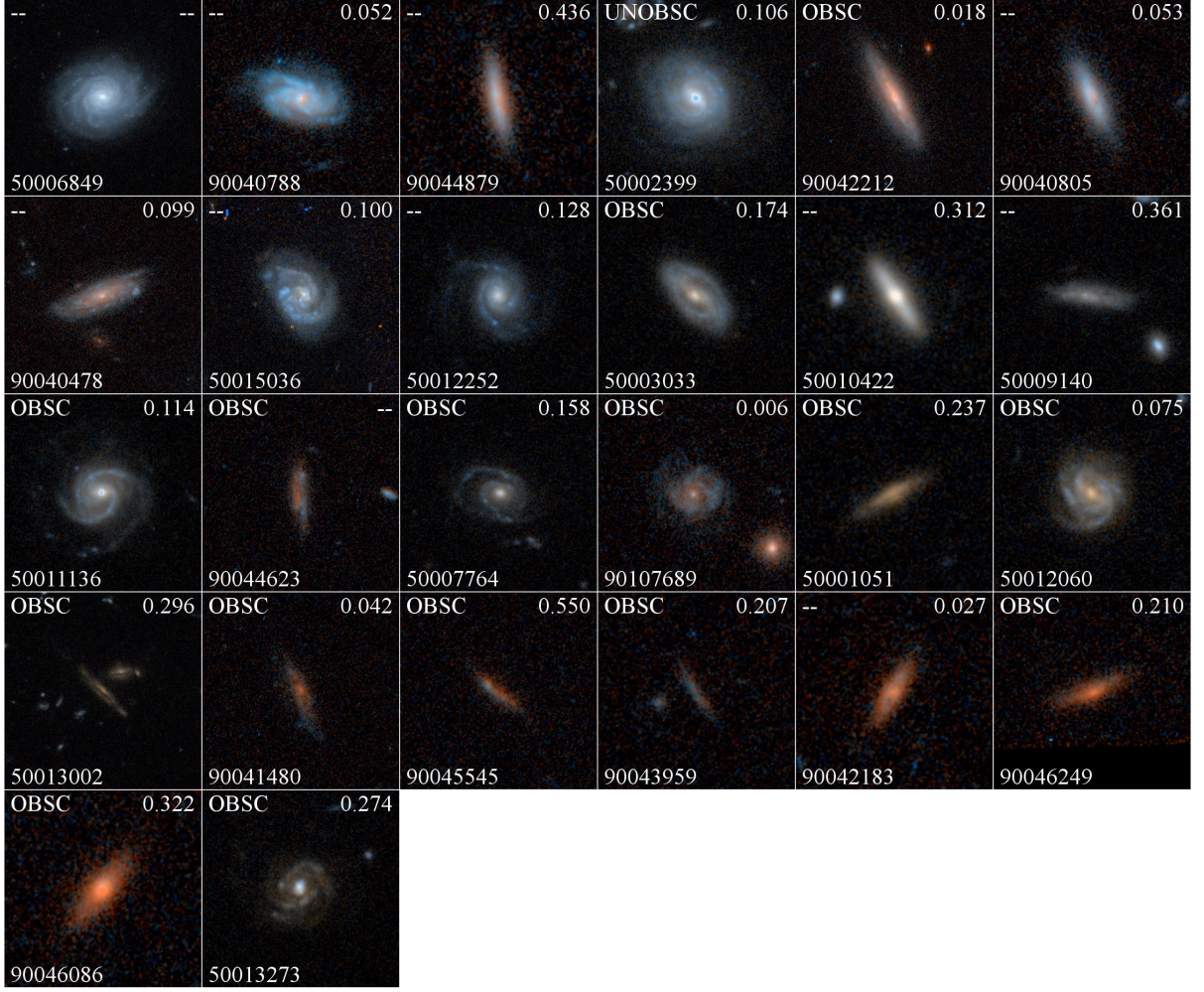


Figure 1: Galaxy Zoo [27] colour images of 26 candidate bulgeless AGN hosts, sorted by ascending redshifts. AGN classifications, and bulge-to-disk luminosity ratios are inscribed in the top left and top right corner respectively. Object 50006849 contains a classical bulge and 90044623 could not be decomposed by parametric fitting. Both were removed from the sample. Of the remaining 24 galaxies, 15 objects contain X-ray confirmed obscured (OBSC) or unobscured (UNOBS) AGN. 13 contain pseudo-bulge contributions of $> 15\%$, the other 11 are predominantly bulgeless, indicating that all 24 galaxies have a merger-free history.

but not necessarily a pseudo-bulge.

Parametric fitting of a Sérsic profile (see Section 3.3.1) to a bulge can be used to distinguish classical bulges from pseudo-bulges. An exponential disk profile has Sérsic index $n = 1$, whereas a de Vaucouleurs elliptical has $n = 4$ [34]. It has been shown that almost all classical bulges have $n \geq 2$ [35], and although some pseudo-bulges might have $n \approx 4$, the $n < 2$ criterion employed in this project should be a reliable sufficient condition for characterising pseudo-bulges [33].

3.3 Parametric morphological fitting using GALFIT

Parametric morphological fitting was performed with GALFIT, developed by Peng et al [34] [36], which can simultaneously fit an arbitrary number of components to an image, including offset components such as companion galaxies. The user specifies initial guesses for these components, and GALFIT will determine the best-fit parameters in an iterative procedure using a χ^2 minimisation algorithm.

GALFIT produces three output images, as well as a log file containing final fit parameters.

ters and uncertainties. An example of these is presented in Figure 2 for object 50002399. The first output image is the original input image cut to the size of the fitting region, and the second image is the best fit model. The third image contains the “residuals”, i.e. the model subtracted from the first image.

Detailed modelling of spiral arms and bars was not required for the purposes of this project, so all components used in this project were axisymmetric and smooth. The following sections explain details of these components.

3.3.1 Sérsic profile

The Sérsic light profile for fitting disks and bulges has the following functional form:

$$\Sigma(r) = \Sigma_e \exp \left[-\kappa \left(\left(\frac{r}{r_e} \right)^{1/n} - 1 \right) \right] \quad (1)$$

$\Sigma(r)$ gives the pixel surface brightness at radius r , and Σ_e gives the pixel surface brightness at the effective radius r_e . The effective radius is defined such that half the flux falls within r_e . n is the Sérsic index, and quantifies how concentrated the light distribution in the core is compared to that in the outer regions, with $n = 1$ corresponding to an exponential disk, and $n = 4$ to a de Vaucouleurs elliptical.[34]. Given these constraints from Σ_e , r_e and n , the value of κ is fixed for a given n . **GALFIT** can also fit Sérsic profiles at an angle to the direction of view. The Sérsic profile has been implemented with the following free parameters: position coordinates x and y , integrated magnitude, effective radius, Sérsic index, axis ratio (b/a), position angle.

3.3.2 Point Spread Function (PSF)

The point spread function (PSF) quantifies the response of the imaging system to a point source. **GALFIT** requires a convolution PSF image provided by the user. The PSFs used in this project are empirical PSFs for each field (HDF-N and CDF-S) and band (I and V), created by the GOODS team and based on ~ 30 stars each. **GALFIT** requires 3 free parameters for the PSF: x and y coordinates, and total magnitude.

3.3.3 Background Sky

The sky background allows the user to model either a fixed constant background value across the image, or to vary this value in both the x and y directions to simulate the atmosphere. In this case, as the images were taken by the *HST*, there are no atmospheric effects to subtract, so the x and y tilt were set to zero. As a result the sky had only the background pixel as a free parameter. Physically, this background results from scattered light and instrument noise that has not been fully subtracted in the reduction.

3.4 Morphological fitting and AGN-host decomposition

3.4.1 General fitting procedures

An initial run of automated fitting was performed using input files with guesses based on the Advanced Camera for Surveys General Catalog (ACS-GC)[37]. These values were obtained from automated fits with a single Sérsic profile, and it is interesting to note that in many cases I found that these were significantly improved throughout the fitting procedure as I used more sophisticated models (see Section 4). For this first run the initial Sérsic index was set to $n = 2$ in all input files, to avoid imposing bias towards either an elliptical or a disk profile. The total flux was divided equally among the PSF and disk.

During the automated run crashes occurred for several objects. The most common problem was that the initial guesses for the sky parameter were almost invariably too high by several orders of magnitude. This was resolved by initially setting the sky to zero and zooming out several times. This allowed **GALFIT** to let the sky convert to its real (significantly smaller) background value away from light sources. Another problem in some cases was the presence of companions or artefacts. Section 3.4.2 explains how these were taken care of.

After repairing these crashes, I manually improved upon each fit via individual follow-up fitting. After finding the best possible fits within the disk and PSF model, I proceeded to add bulges. In many cases, the addition of bulges significantly improved the fit, and often the addition of a bulge solved problems with

the previous disk and PSF models. For instance, in most face on galaxies, n was unnecessarily high and central residuals were poor due to the presence of a small central (pseudo-)bulge. **GALFIT** tried to reconstruct this feature in a single disk component by making the light distribution more central, thus increasing n . Adding bulges improved both the disk n and central residuals. A summary of commonly encountered issues that arose throughout the entire iterative follow-up process, and details on how they were dealt with, is provided in Section 3.4.2. An example of the best fit of object 50002399 is provided in Figure 2 and Table 1.

During fitting, in addition to the χ^2 parameter, I adopted the following characteristics as indicative of a good fit:

- *Constant residuals*: even residuals, where neither oversubtraction nor undersubtraction occurs, indicate a good fit. The maximum extend to which this is possible, however, depends on the smoothness of the light distribution in each galaxy image.
- *Sensible parameters*: parameters were required to be in good accordance with expectations from visually inspecting input images. For example, most galaxies are known to have Sérsic indices of between 0.1 and 8 [38]. Therefore, when the Sérsic index converged to a value outside this range, n was fixed to a sensible value. In cases where parameters were fixed, care was taken to ensure the fit recovered the maximum bulge luminosity in order to obtain a secure upper limit on bulge flux.
- *Match between bulge and disk*: as bulges are mostly axisymmetric around the same axis as the disk they live in, they should undergo very similar projection and orientation effects. The axis ratio parameter, for instance, is mainly a result of projection (a disk will appear oval due to the inclination of its central axis). Consequently bulge and disk axis ratios and position angles, as well as positions, are expected to be similar, and were constrained to be if not.

3.4.2 Individual fitting challenges

Following the above procedures would generate optimal fits in the case of smooth and featureless galaxies in images without artifacts. However, the sample considered in this project was specifically selected to contain disk-dominated galaxies, which often have detailed or asymmetric features that require careful treatment. This section summarises the main issues that arose during fitting, and how they were handled.

Firstly, an important common issue involved companion galaxies with light profiles intersecting those of the main galaxy. In cases where these companions were of considerable size I fit them simultaneously with the main galaxy, in order to ensure that the extended wings of the companion’s light profile were not confused with the main galaxy.

Secondly, many galaxies contained irregular features. Spiral arms for instance, could lead to chaotic residuals with both over- and under-subtracted regions. However, this in itself need not generate poor disk luminosities. **GALFIT** generally handles brightness contrast well as part of the optimisation procedure, as long as the image does not contain extremely bright or dark features. To this end, exceptionally bright parts such as starburst regions were masked out. Bars, on the other hand, could lead to incorrect fits, as **GALFIT** would attempt to reconstruct them by rotating and narrowing the sersic profiles of disks or bulges in order to create a narrow central region. In order to avoid this, I often constrained the axis ratios and position angles of bulge and disk to be similar.

Thirdly, in some cases dust led to apparent disk asymmetry and obscuration, as exemplified by object 50013002. **GALFIT** does not currently model any components with negative or absorbed luminosity, so optimisation of images containing prominent dust lanes will always lead to erroneously low luminosities, or in worse cases, reproduction of dust induced asymmetry or failure to correctly reproduce obscured features. Theoretically, one could apply a bad pixel mask to dust dominated regions, which forces **GALFIT** to ignore the pixels within the masked region. However, in practice it often turned out that this only amplified obscuration issues. Thus dust masks were



Figure 2: GALFIT output for i-band imaging of object 50002399 and a companion. Left: Input image cropped to fit box size. Middle: best fit model containing disk, bulge and PSF components. Right: residuals obtained from subtracting the latter from the former. Even though forcing an axisymmetric model to non-axisymmetric bars leads to strong undersubtraction of the bar features and oversubtraction of the surrounding area, the residuals indicate these contributions are well balanced. Most importantly, the residuals demonstrate the outer regions of the disk are well subtracted, resulting in the most accurate disk profile over the entire region.

	x (pix)	y (pix)	m	r_e (pix)	n	b/a	P.A. (degrees)
Disk	501.79	502.02	19.24	32.09	1.14	[0.92]	43.28
Bulge	[501.00]	[501.83]	21.56	5.08	0.37	[0.92]	[45.26]
Companion	413.73	617.55	22.28	17.01	0.82	0.90	-50.07
PSF	501.01	501.88	20.69				
<hr/>							
Sky: 6.59e-04	χ^2 : 396480		N_{dof} : 130301				

Table 1: Output GALFIT parameters for the best fit of object 50002399. At the redshift of this source each pixel corresponds to 0.22 kpc, so the effective radii are $r_e \sim 7$ kpc and $r_e \sim 1$ kpc for the disk and bulge respectively. Parameter values enclosed in square brackets have been held fixed. The disk axis ratio (b/a) was held fixed, and bulge x and y , b/a and position angle (P.A.) were fixed to similar values as the disk, in order to prevent GALFIT from modifying these components to reproduce the non-axisymmetric bar component.

avoided where possible. Instead, parameter constraints (e.g. equating bulge and disk centres) were employed to combat asymmetries if necessary.

Finally, a number of images contained artifacts, or diffraction spikes. These issues were easily avoided by applying a bad pixel mask.

Despite these caveats I eventually obtained a reasonable best fit for all objects, apart from object 90044623, where dust effects prevented a convergence to reasonable physical values (see Table 2).

4 RESULTS

4.1 GALFIT results

Best fit parameters for all 26 candidate objects are presented in Table 2. I renormalised magnitudes to the well measured values from GOODS[37], and obtained errors on the GALFIT parameters following Simmons & Urry 2008 [29]. Because these errors are derived from automated batch fitting, they form very conservative upper limits. My sample has been carefully individually fit, and actual errors are likely to be much smaller.

The n_{blg} value for object 50006849 indicates a classical bulge, so this object was removed from the mergerless sample. Object 90044623 was rejected for having unphysical fit

OBJNO	z	GALFIT parameters (I -band)				$\frac{L_{blg}}{L_{host}}$	Significance		$\log M(M_{\odot})$	
		m_{disk}	n_{disk}	m_{blg}	n_{blg}		σ_{PS}	σ_{blg}	M_{BH}	M_{host}
50006849	0.137	17.84 $^{+0.18}_{-0.18}$	1.35 $^{+0.29}_{-0.29}$	20.46 $^{+0.07}_{-0.07}$	2.66 $^{+0.20}_{-0.20}$	0.082	6	6	3.3	9.6
90040788	0.204	19.33 $^{+0.27}_{-0.27}$	0.66 $^{+0.29}_{-0.29}$	22.48 $^{+0.07}_{-0.07}$	1.15 $^{+0.20}_{-0.20}$	0.052	6	6	3.8	9.2
90044879	0.2363	21.92 $^{+0.23}_{-0.23}$	0.59 $^{+0.33}_{-0.33}$	22.20 $^{+0.16}_{-0.16}$	0.35 $^{+0.27}_{-0.27}$	0.436	6	6	3.5	9.1
50002399	0.3059	19.30 $^{+0.33}_{-0.33}$	1.14 $^{+0.29}_{-0.29}$	21.62 $^{+0.31}_{-0.31}$	0.37 $^{+0.25}_{-0.25}$	0.106	6	6	6.3	9.7
90042212	0.31	18.98 $^{+0.31}_{-0.31}$	1.85 $^{+0.25}_{-0.25}$	23.30 $^{+0.07}_{-0.07}$	0.23 $^{+0.20}_{-0.20}$	0.018	6	6	4.6	10.1
90040805	0.316	20.30 $^{+0.28}_{-0.28}$	1.02 $^{+0.28}_{-0.28}$	23.43 $^{+0.07}_{-0.07}$	0.55 $^{+0.16}_{-0.16}$	0.053	6	6	4.2	9.2
90040478	0.338	19.29 $^{+0.28}_{-0.28}$	0.54 $^{+0.28}_{-0.28}$	21.69 $^{+0.09}_{-0.09}$	0.94 $^{+0.22}_{-0.22}$	0.099	6	6	4.1	9.8
50015036	0.375	19.09 $^{+0.29}_{-0.29}$	0.64 $^{+0.27}_{-0.27}$	21.47 $^{+0.12}_{-0.12}$	0.35 $^{+0.24}_{-0.24}$	0.100	6	6	4.4	9.5
50012252	0.3766	20.62 $^{+0.29}_{-0.29}$	1.24 $^{+0.27}_{-0.27}$	22.70 $^{+0.14}_{-0.14}$	0.41 $^{+0.26}_{-0.26}$	0.128	6	6	4.9	9.0
50003033	0.411	20.63 $^{+0.28}_{-0.28}$	0.30 $^{+0.28}_{-0.28}$	22.32 $^{+0.14}_{-0.14}$	0.87 $^{+0.26}_{-0.26}$	0.174	6	6	4.4	9.4
50010422	0.4725	21.09 $^{+0.33}_{-0.33}$	0.61 $^{+0.25}_{-0.25}$	21.95 $^{+0.27}_{-0.27}$	0.35 $^{+0.29}_{-0.29}$	0.312	6	6	4.3	9.3
50009140	0.4745	22.12 $^{+0.21}_{-0.21}$	0.29 $^{+0.31}_{-0.31}$	22.74 $^{+0.12}_{-0.12}$	1.00 $^{+0.24}_{-0.24}$	0.361	6	6	4.2	8.7
50011136	0.5124	20.07 $^{+0.33}_{-0.33}$	0.60 $^{+0.29}_{-0.29}$	22.30 $^{+0.31}_{-0.31}$	0.12 $^{+0.25}_{-0.25}$	0.114	6	6	6.7	9.5
90044623	0.576	22.64 $^{+0.07}_{-0.07}$	0.38 $^{+0.20}_{-0.20}$	21.93 $^{+0.06}_{-0.06}$	9.84 $^{+0.09}_{-0.09}$	0.658	6	6	4.6	9.0
50007764	0.5951	21.28 $^{+0.24}_{-0.24}$	1.13 $^{+0.32}_{-0.32}$	23.10 $^{+0.07}_{-0.07}$	0.86 $^{+0.20}_{-0.20}$	0.158	6	6	5.0	9.0
90107689	0.622	21.14 $^{+0.29}_{-0.29}$	0.57 $^{+0.37}_{-0.37}$	26.73 $^{+0.21}_{-0.21}$	0.10 $^{+0.31}_{-0.31}$	0.006	6	4	4.9	9.0
10001051	0.634	22.97 $^{+0.24}_{-0.24}$	0.69 $^{+0.32}_{-0.32}$	24.24 $^{+0.12}_{-0.12}$	0.49 $^{+0.24}_{-0.24}$	0.237	5	6	5.6	9.4
50012060	0.6378	20.73 $^{+0.28}_{-0.28}$	0.68 $^{+0.28}_{-0.28}$	23.45 $^{+0.07}_{-0.07}$	0.97 $^{+0.20}_{-0.20}$	0.075	6	6	5.2	9.7
50013002	0.6379	21.77 $^{+0.07}_{-0.07}$	0.50 $^{+0.20}_{-0.20}$	22.71 $^{+0.07}_{-0.07}$	0.90 $^{+0.20}_{-0.20}$	0.296	4	6	6.0	9.7
90041480	0.6432	21.49 $^{+0.21}_{-0.21}$	0.64 $^{+0.31}_{-0.31}$	24.89 $^{+0.07}_{-0.07}$	0.63 $^{+0.20}_{-0.20}$	0.042	1	6	4.5	9.3
90045545	0.654	23.3 $^{+0.14}_{-0.14}$	0.30 $^{+0.26}_{-0.26}$	23.08 $^{+0.07}_{-0.07}$	0.50 $^{+0.20}_{-0.20}$	0.550	6	6	4.7	9.2
90043959	0.6741	23.81 $^{+0.16}_{-0.16}$	0.35 $^{+0.27}_{-0.27}$	25.27 $^{+0.07}_{-0.07}$	0.13 $^{+0.20}_{-0.20}$	0.207	0	6	4.5	8.3
90042183	0.7213	22.25 $^{+0.35}_{-0.35}$	0.95 $^{+0.27}_{-0.27}$	26.13 $^{+0.16}_{-0.16}$	0.14 $^{+0.27}_{-0.27}$	0.027	6	6	5.2	9.8
90046249	0.734	22.43 $^{+0.21}_{-0.21}$	0.7 $^{+0.31}_{-0.31}$	23.87 $^{+0.05}_{-0.05}$	0.88 $^{+0.18}_{-0.18}$	0.210	0	5	6.6	10.0
90046086	0.7373	22.05 $^{+0.28}_{-0.28}$	0.71 $^{+0.28}_{-0.28}$	22.86 $^{+0.21}_{-0.21}$	0.78 $^{+0.31}_{-0.31}$	0.322	6	6	5.2	10.4
50013273	0.9712	21.62 $^{+0.32}_{-0.32}$	0.58 $^{+0.24}_{-0.24}$	22.68 $^{+0.24}_{-0.24}$	0.11 $^{+0.32}_{-0.32}$	0.274	6	6	5.3	10.2

Table 2: Properties of the sample of 26 bulgeless candidates sorted by ascending redshift. Values for m_{disk} , $r_{e,disk}$, n_{disk} , m_{blg} , $r_{e,blg}$ and n_{disk} were obtained with GALFIT from I -band imaging. Conservative errors on these values have been obtained from Simmons & Urry 2008 [29]. Fit parameters demonstrate that object 90044623 could not be fit correctly and that object 50006849 contains a classical bulge. Both are indicated in red and were removed from the sample. 13 galaxies have sizeable pseudobulges of $L_{blg}/L_{tot} > 0.15$, with the other 11 galaxies being predominantly bulgeless. σ_{psf} and σ_{blg} quantify the significance of adding a psf or bulge respectively. Black hole masses are lower limits based on Eddington limit accretion. Disk masses have been calculated following Bell & De Jong 2001 [39]

parameters. 13 galaxies contain a significant pseudo-bulge contribution $L_{blg}/L_{host} > 0.15$, the other 11 are predominantly bulgeless.

I computed disk masses following Bell & de Jong [39] with K-corrections from Poggianti [40], the details of which are provided in Appendix A.

σ_{PS} and σ_{blg} quantify the statistical significance of adding a point source or bulge component to the model respectively. These values have been obtained from an F-test and indicate the amount of standard deviations by which the more sophisticated model improves

on the simpler one. Details of this procedure are provided in Appendix B.

It is interesting to note that the best fit parameters in Table 2 differ significantly from the values obtained for a single Sérsic profile in the ACS-GC [37]. The vast majority of ACS-GC fits have significantly higher n values, on average ~ 1.3 higher. The difference is most extreme in the case of object 50002399, where the AGN-GC value is 6.32 too high. These results are expected, since in a single disk model, GALFIT will attempt to reconstruct a point source by centralising the light profile, thus

increasing n . Additionally, in Section 3.4.1 I noted how several fits improved significantly from the addition of bulges. Together these results demonstrate the importance of sophisticated models in automated fitting procedures, indicating the need to model both disk, bulge and PSF in order to properly extract galaxy morphologies in the case of active galaxies.

4.2 Black hole masses

The Eddington limit is the maximum bolometric luminosity an accreting BH can achieve when radiation pressure emitted from accreting matter is in hydrostatic equilibrium with the gravitational pull exerted by the black hole. At the Eddington limit, there is a relation between mass and luminosity [41]:

$$L_{edd} = 1.3 \cdot 10^{38} \left(\frac{M_{edd}}{M_{\odot}} \right) \frac{\text{erg}}{\text{sec}} \quad (2)$$

If the bolometric luminosity is assumed to be the Eddington luminosity, Equation 2 gives a lower bound on the black hole mass. This can be seen by considering the fact that if the observed luminosity is below the Eddington limit, it is lower than the maximum value that can still be contained by gravity. If the observed luminosity stays the same, this implies that the gravitational pull of the black hole must be stronger for the black hole to be able to gravitationally counteract the radiation pressure, implying a higher black hole mass.

I used bolometric luminosities obtained from X-ray hard band luminosities to compute Eddington limit lower bounds on black hole masses. These lower limits are quite conservative, as most black holes accrete well below their Eddington limit. For instance, the AGN in Simmons et al. 2013 with firm black hole masses had a mean of $L \approx 0.065 L_{Edd}$ [7]. I used this value to obtain an indication of the more probable real value of the black hole masses. It must be noted, however, that 8 X-ray hard band luminosities were only provided as upper limits. In these cases, it is possible that the Eddington limit masses are not a secure lower limit, as the bolometric luminosities could in fact be lower. In all subsequent figures these objects were marked by an inverted triangle.

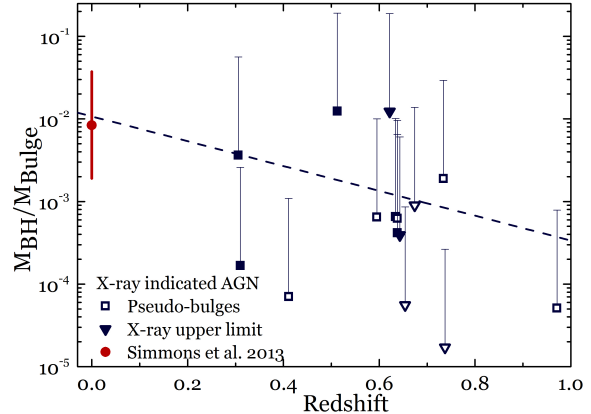


Figure 4: Ratio of black hole to bulge mass as a function of redshift, for all 15 X-ray detected AGN. Of these, 8 hosts contain sizeable pseudo-bulges ($L_{bulge}/L_{host} > 0.15$), the remaining 7 are predominantly bulgeless. In the case of triangular markers, X-ray luminosities were an upper limit, so for these, the Eddington limit masses could be too high. The dashed line indicates the best fit for these 14 hosts. The average value found in Simmons et al. 2013 for $z \sim 0$ is shown in red and falls neatly onto the relation. Including it does not change the best fit, but halves the errors resulting in a best fit of $\log(\frac{M_{BH}}{M_{bulge}}) = -2.0(\pm 0.5) - 1.4(\pm 0.9)z$. These results hint that over time, black holes “outgrow” their pseudo-bulges.

Black hole mass relations using the results in this section are displayed in Figure 3 and Figure 4.

5 DISCUSSION

As mentioned in Section 1, according to current galaxy formation theories, galaxies are built up hierarchically through a series of mergers, which are also thought to be responsible for the growth of supermassive black holes. In this picture, where the coevolution of hosts and their black holes is driven by mutual growth through mergers, large mergerless galaxies with SMBHs are expected to be rare. Moreover, considering the fact that only a small fraction of SMBHs is in an actively growing phase, mergerless AGN hosts are predicted to be even rarer. Nevertheless I have identified 24 such galaxies, of which 11 are pre-

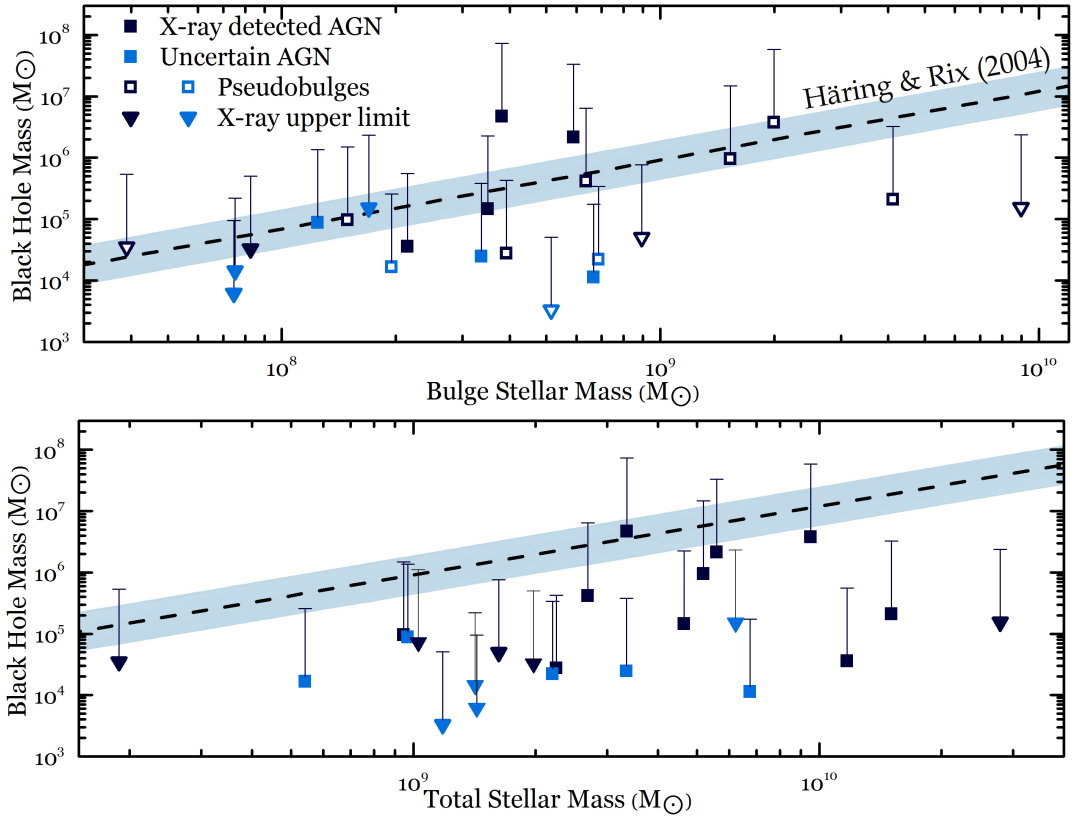


Figure 3: Black hole mass versus bulge mass (top) and total stellar host galaxy stellar mass (bottom). Black hole masses are lower bounds assuming Eddington limit accretion, caps indicate more likely black hole masses assuming an Eddington ratio of 0.065. The 10 galaxies with sizeable ($L_{bulge}/L_{host} > 0.15$) pseudo-bulges are indicated by open markers, whereas the remaining 15 bulgeless galaxies are indicated by solid markers. Triangular markers show objects for which X-ray luminosities are an upper limit, implying that the M_{BH} lower bounds on these objects could possibly be *lower*. Light blue data points designate objects for which AGN selection criteria[?] did not indicate a likely AGN and these could constitute star formation galaxies. Both plots demonstrate a tentative agreement with the relation between bulge/elliptical stellar mass and black hole mass from Häring & Rix 2004 [15] indicated by the dashed line. Especially if less importance is attached to the uncertain AGN, black hole mass limits are mostly consistent with the Häring & Rix relation within its 0.3 dex scatter, if the relation is assumed to hold for bulge and total stellar mass.

dominantly bulgeless (pseudo-bulge contribution of $< 0.15\%$), and the other 13 contain more sizeable pseudo-bulges. Despite the fact that pseudo-bulges are indicative of a slightly violent history including strong disk instabilities such as bars and clumps, they are still formed in merger-free processes [42], implying a merger-free history for all 24 objects. This project thus adds to the local sample of mergerless AGN hosts found in Simmons et al. 2013, strengthening the case for black hole growth independent of mergers. Furthermore, the galaxies in this sample follow the same quantitative mass relations as merger-

dominated classical bulges and ellipticals (see Figure 3).

It must be noted that the results presented here have a several limitations in their accuracy. First of all, the k-corrections were performed under likely unrealistically simple assumptions, and different methods could give a factor of 2 (0.3 dex) offset in disk mass. Furthermore, bulge masses were computed with the aim of maximising any possible bulge contribution, so should be read as a secure upper limit on bulge mass. On top of this, as mentioned in section 4.2, X-ray catalogs merely provided an upper limit on the point source

flux for 8 objects. In these cases it is possible that the actual point source luminosity is lower, which would result in a lower Eddington limit, as implied by Equation 2.

5.1 Black hole-bulge relations

Nevertheless, even with these limitations in mind, Figure 3 indicates agreement with earlier relations. Häring & Rix [15] found a local relation between bulge mass and black hole mass applicable to classical bulges, indicated by the dashed line with the 0.3 dex observed scatter in light blue. Within the black hole mass limits, the relations between M_{BH} and pseudo-bulge M_{bulge} observed in this project agree fairly well with this relation, especially disregarding galaxies indicated in light blue, which do not have X-ray indicated AGN. This conclusion disagrees with local results found in Simmons et al. [7], where all lower limits on the black hole mass are higher than expected from Häring & Rix. This trend towards higher M_{BH}/M_{bulge} for descending z is also observed throughout the redshift range of the current sample. Figure 4 illustrates the relation between M_{BH}/M_{bulge} and redshift. The local average result for Simmons et al. is in good agreement with the best fit from my results. Figure 4 tentatively suggests that black holes can accrete mass over time disproportionately to their pseudo-bulges, which would imply calm BH-accretion independently of galaxy mergers, but also of dynamical processes that grow pseudo-bulges.

Furthermore, it is interesting to note the average disk mass in Simmons et al. is $M_{BH} = 1.51 \times 10^{10} M_{\odot}$ for an average redshift of $z = 0.036$. To compare, the average disk mass in my sample is $M_{BH} = 4.74 \times 10^9 M_{\odot}$ for an average redshift of $z = 0.509$. If my sample is hypothesised to be the progenitors of the Simmons et al. sample, this would imply a star formation rate of $1 M_{\odot}/\text{year}$, which is a very typical value [43]. Care must be taken regarding the interpretation of this result, as pseudo-bulge sizes for part of my sample precludes these galaxies from being progenitors of the Simmons et al. galaxies, which barely contain pseudo-bulges at all. My other 11 bulgeless galaxies though, are consistent with having evolved into galaxies like in Simmons et al, a hypothesis which, if true, could explain the

redshift trend observed in 4.

5.2 Black hole-host relations

If the Häring & Rix relation is extended to include total stellar mass as well as bulge mass, it would describe elliptical galaxies, as elliptical galaxies have similar light profiles (and consequently mass profiles assuming a constant mass-to-light ratio) to large classical bulges. Notably the current sample of mergerless disk galaxies also largely follows this predicted relation for elliptical galaxies, as indicated by Figure 3. Simmons et al. 2013 found a similar agreement. Plots of M_{BH}/M_{host} versus redshift show no significant slope and are consistent with the relation being flat. Such a flat redshift dependence has earlier been observed for merger dominated ellipticals and galaxies with significant classical bulges [44][45]. The fact that mergerless galaxy follow the same black hole-disk mass relations as expected for merger dominated elliptical galaxies, (and possibly even the same redshift dependence) suggests that mergers may not be the fundamental process driving this galaxy-SMBH coevolution.

6 CONCLUSION

Of a candidate sample of 26 bulgeless AGN candidates, parametric morphological fitting indicated that, 11 are predominantly bulgeless, with bulge contributions of less than 15%. The other 13 objects have significant pseudo-bulges, implying that a merger-free history for all 24 galaxies. 15 galaxies host X-ray indicated AGN. For the others the presence of an AGN is uncertain, as X-ray emission did not indicate AGN presence, but parametric fitting did detect significant central point sources. This project thus establishes a secure sample of 15 (possibly 24) mergerless AGN hosts, indicating that significant SMBH growth is possible in the absence of mergers.

Furthermore, these mergerless galaxies obey similar relations between black hole mass, and disk and bulge mass as classical bulges and ellipticals, implying that merger processes need not be central to the coevolution of galaxies and black holes. The data also indicate a relationship between the ratio of black hole mass to pseudo-bulge mass (M_{BH}/M_{bulge}) and red-

shift, suggesting that black hole masses grow as time progresses, eventually “outgrowing” their pseudo-bulges. This might imply that over time black holes might accrete independently of processes that form pseudo-bulges, as well as independently of mergers.

In order to strengthen the conclusions above, I would recommend to improve the precision of bulge luminosities, as I computed these rather conservatively. A possible suggestion to this end would be to perform parametric fitting in multiple bands simultaneously, using a multi-band version of GALFIT that will soon be publicly available [46]. Furthermore, future work could concentrate on implementing more sophisticated models of k-corrections in order to improve disk mass estimates.

More generally, the most significant advancement on this project would be to extend the sample size, for instance by adding bulgeless galaxies from other surveys such as COSMOS [47] and AEGIS [48]. Significant progress could be made if one could find a way to detect bulgeless AGN host galaxies in large surveys by performing automated fitting of models with disk, bulge and PS components. However, the difficulties encountered in this project when trying to optimise such sophisticated fits on galaxies with irregular features suggest that it might be difficult to implement such a procedure on a large scale.

References

- [1] D. B. Sanders, et al. Ultraluminous infrared galaxies and the origin of quasars. *"Astrophys. J."*, 325:74–91, February 1988.
- [2] P. F. Hopkins, et al. A Cosmological Framework for the Co-Evolution of Quasars, Supermassive Black Holes, and Elliptical Galaxies. I. Galaxy Mergers and Quasar Activity. *"Astrophys. J., Suppl. Ser."*, 175:356–389, April 2008.
- [3] D. J. Croton, et al. The many lives of active galactic nuclei: cooling flows, black holes and the luminosities and colours of galaxies. *"Mon. Not. R. Astron. Soc."*, 365:11–28, January 2006.
- [4] K. Schawinski, et al. HST WFC3/IR Observations of Active Galactic Nucleus Host Galaxies at $z \sim 2$: Supermassive Black Holes Grow in Disk Galaxies. *"Astrophys. J., Lett."*, 727:L31, February 2011.
- [5] D. D. Kocevski, et al. CANDELS: Constraining the AGN-Merger Connection with Host Morphologies at $z \sim 2$. *"Astrophys. J."*, 744:148, January 2012.
- [6] B. D. Simmons, et al. Moderate-luminosity Growing Black Holes from $1.25 < z < 2.7$: Varied Accretion in Disk-dominated Hosts. *"Astrophys. J."*, 761:75, December 2012.
- [7] Brooke D. Simmons, et al. Galaxy Zoo: bulgeless galaxies with growing black holes. *Monthly Notices of the Royal Astronomical Society*, 429(3):2199–2211, 2013.
- [8] J. Binney et al. *Galactic dynamics*. 1987.
- [9] J. Magorrian, et al. The Demography of Massive Dark Objects in Galaxy Centers. *"Astron. J."*, 115:2285–2305, June 1998.
- [10] A. Marconi, et al. Local supermassive black holes, relics of active galactic nuclei and the X-ray background. *"Mon. Not. R. Astron. Soc."*, 351:169–185, June 2004.

- [11] D. Lynden-Bell. Galactic Nuclei as Collapsed Old Quasars. *"Nature"*, 223:690–694, August 1969.
- [12] A. Cavaliere et al. The connection between active and normal galaxies. *"Astrophys. J., Lett."*, 340:L5–L8, May 1989.
- [13] K. Gebhardt, et al. A Relationship between Nuclear Black Hole Mass and Galaxy Velocity Dispersion. *"Astrophys. J., Lett."*, 539:L13–L16, August 2000.
- [14] A. Marconi et al. The Relation between Black Hole Mass, Bulge Mass, and Near-Infrared Luminosity. *"Astrophys. J., Lett."*, 589:L21–L24, May 2003.
- [15] Nadine Haring et al. On the black hole mass - bulge mass relation. *Astrophys. J.*, 604:L89–L92, 2004.
- [16] M. Dickinson, et al. The Great Observatories Origins Deep Survey. In R. Bender et al., editors, *The Mass of Galaxies at Low and High Redshift*, page 324, 2003.
- [17] M. Giavalisco, et al. The Great Observatories Origins Deep Survey: Initial Results from Optical and Near-Infrared Imaging. *"Astrophys. J., Lett."*, 600:L93–L98, January 2004.
- [18] J. Kormendy et al. Secular Evolution and the Formation of Pseudobulges in Disk Galaxies. *"Ann. Rev. Astron. Astrophys."*, 42:603–683, September 2004.
- [19] D. M. Alexander, et al. The Chandra Deep Field North Survey. XIII. 2 Ms Point-Source Catalogs. *"Astron. J."*, 126:539–574, August 2003.
- [20] Y. Q. Xue, et al. The Chandra Deep Field-South Survey: 4 Ms Source Catalogs. *"Astrophys. J., Suppl. Ser."*, 195:10, July 2011.
- [21] C. N. Cardamone, et al. Mid-Infrared Properties and Color Selection for X-Ray-Detected Active Galactic Nuclei in the MUSYC Extended Chandra Deep Field-South. *"Astrophys. J."*, 680:130–142, June 2008.
- [22] F. E. Bauer, et al. The Chandra Deep Field North Survey. XII. The Link between Faint X-Ray and Radio Source Populations. *"Astron. J."*, 124:2351–2363, November 2002.
- [23] F. E. Bauer, et al. The Fall of Active Galactic Nuclei and the Rise of Star-forming Galaxies: A Close Look at the Chandra Deep Field X-Ray Number Counts. *"Astron. J."*, 128:2048–2065, November 2004.
- [24] G. D. Wirth, et al. The Team Keck Treasury Redshift Survey of the GOODS-North Field. *"Astron. J."*, 127:3121–3136, June 2004.
- [25] L. L. Cowie, et al. A Large Sample of Spectroscopic Redshifts in the ACS-GOODS Region of the Hubble Deep Field North. *"Astron. J."*, 127:3137–3145, June 2004.
- [26] A. J. Barger, et al. A Highly Complete Spectroscopic Survey of the GOODS-N Field1,. *"Astrophys. J."*, 689:687–708, December 2008.
- [27] T. Melvin, et al. Galaxy Zoo: are we observing an epoch of bar formation in massive disk galaxies?. *Memorie della Societa Astronomica Italiana Supplementi*, 25:82, 2013.
- [28] G. P. Szokoly, et al. The Chandra Deep Field-South: Optical Spectroscopy. I.
- [29] B. D. Simmons et al. The Accuracy of Morphological Decomposition of Active Galactic Nucleus Host Galaxies. *"Astrophys. J."*, 683:644–658, August 2008.
- [30] D. Tody. IRAF in the Nineties. In R. J. Hanisch, et al., editors, *Astronomical Data Analysis Software and Systems II*, volume 52 of *Astronomical Society of the Pacific Conference Series*, page 173, January 1993.
- [31] M. B. Taylor.
- [32] R Core Team. *R: A Language and Environment for Statistical Computing*. R Foundation for Statistical Computing, Vienna, Austria, 2014.

- [33] John Kormendy et al. Coevolution (or not) of supermassive black holes and host galaxies. *Annual Review of Astronomy and Astrophysics*, 51(1):511–653, 2013.
- [34] Chien Y. Peng, et al. Detailed structural decomposition of galaxy images. *Astron.J.*, 124:266–293, 2002.
- [35] D. B. Fisher et al. Bulges of Nearby Galaxies with Spitzer: Scaling Relations in Pseudobulges and Classical Bulges. *"Astrophys. J."*, 716:942–969, June 2010.
- [36] Chien Y. Peng, et al. Detailed Decomposition of Galaxy Images. II. Beyond Axisymmetric Models. *Astron.J.*, 139:2097–2129, 2010.
- [37] R. L. Griffith, et al. The Advanced Camera for Surveys General Catalog: Structural Parameters for Approximately Half a Million Galaxies. *"Astrophys. J., Suppl. Ser."*, 200:9, May 2012.
- [38] N. Caon, et al. On the Shape of the Light Profiles of Early Type Galaxies. *"Mon. Not. R. Astron. Soc."*, 265:1013, December 1993.
- [39] E. F. Bell et al. Stellar Mass-to-Light Ratios and the Tully-Fisher Relation. *"Astrophys. J."*, 550:212–229, March 2001.
- [40] B. M. Poggianti. K and evolutionary corrections from UV to IR. *"Astron. Astrophys. Suppl. Ser."*, 122:399–407, May 1997.
- [41] T. J.-L. Courvoisier. *High Energy Astrophysics*. 2013.
- [42] M. Martig, et al. A Diversity of Progenitors and Histories for Isolated Spiral Galaxies. *"Astrophys. J."*, 756:26, September 2012.
- [43] J. Brinchmann, et al. The physical properties of star-forming galaxies in the low-redshift Universe. *"Mon. Not. R. Astron. Soc."*, 351:1151–1179, July 2004.
- [44] M. Cisternas, et al. Secular Evolution and a Non-evolving Black-hole-to-galaxy Mass Ratio in the Last 7 Gyr. *"Astrophys. J., Lett."*, 741:L11, November 2011.
- [45] K. Jahnke et al. The Non-causal Origin of the Black-hole-galaxy Scaling Relations. *"Astrophys. J."*, 734:92, June 2011.
- [46] B. Häußler, et al. MegaMorph - multi-wavelength measurement of galaxy structure: complete Sérsic profile information from modern surveys.
- [47] N. Scoville, et al. The Cosmic Evolution Survey (COSMOS): Overview.
- [48] M. Davis, et al. The All-Wavelength Extended Groth Strip International Survey (AEGIS) Data Sets. *"Astrophys. J., Lett."*, 660:L1–L6, May 2007.

A Host galaxy stellar masses

To compute galaxy total stellar masses from I -band luminosities and $V - I$ colour, I used the following relation from Bell & de Jong 2001 [39] :

$$\log_{10} \left(\frac{M}{L_I} \right) = -1.204 + 1.347(V - I) \quad (3)$$

Here M is the disk mass in solar masses, L_I is the I -band luminosity in solar luminosities. I computed $V - I = m_{v,host} - m_{I,host}$ from I -band and V -band host magnitudes, by combining flux from the bulge and disk. As equation 3 is valid only locally, both $V - I$ and L_I had to be K-corrected for redshift, using K-corrections from Poggianti 1997 [40].

B Statistical significance of point sources

In order to investigate whether adding a component significantly improves the fit an F-test was performed. F values were calculated using:

$$F = \frac{(\chi_{tot}^2 - \chi_i^2)/(0.4N_{dof} - 0.4N_{dof,i})}{(\chi_{tot}^2/0.4N_{dof,tot})} \quad (4)$$

Here ‘ i ’ is a placeholder for either ‘PSF’, giving the F-value for adding a PSF, or ‘bulge’ giving the F-value for bulges. The values for χ_i and N_{dof} were obtained by fitting the best fit model, but with component i removed.

$N_{dof,tot}$ is the number of degrees of freedom indicated by **GALFIT** and is roughly equal to the number of pixels. The factor of 0.4 is required because the number of degrees of freedom output by **GALFIT** does not take into account the fact that the pixel values are already partially constrained by the model. The F-values were compared with the expected value from the null F-distribution (i.e. the distribution that would have been obtained if adding component i would improve the fit). The sigma value displayed in Table 2 indicate how many sigma away the F-values are from the null F-values.